Applications in Energy and Combustion Science 23 (2025) 100342

Contents lists available at ScienceDirect

Applications in Energy and Combustion Science

journal homepage: www.elsevier.com/locate/jaecs

Real-fluid transport property computations based on the Boltzmann-weighted full-dimensional potential model

Xin Zhang [a], Junfeng Bai [c], Bowen Liu [a], Tong Zhu [b,*], Hao Zhao [a,*]

[a] College of Engineering, Peking University, Beijing, 100871, China
[b] School of Chemistry and Molecular Engineering, East China Normal University, Shanghai, 200062, China
[c] Department of Mechanical Engineering, City University of Hong Kong, 999077, Hong Kong

ARTICLE INFO

Keywords:
Real-fluid
Transport property
Intermolecular potential
Non-equilibrium simulation
Supercritical combustion

ABSTRACT

The intermolecular potential plays a crucial role in real-fluid interactions away from the ideal-gas equilibrium, such as supercritical fluid, high-enthalpy fluid, plasma interactions. We propose a Boltzmann-weighted Full-dimensional (BWF) potential model for real-fluid computations. It includes diverse intermolecular interactions so as to determine the potential well, molecular diameter, dipole moment, polarizability of species without introducing bath gases, allowing more accurate descriptions of potential surfaces with more potential parameters. The anisotropy and temperature dependence of potential parameters are also considered by applying the Boltzmann weighting on all orientations. Through the high-level Symmetry-Adapted Perturbation Theory calculations, full-dimensional potential energy surface datasets are obtained in 432 orientations for each species. Subsequently, the Boltzmann-weighted Full-dimensional potential parameters are derived by training the dataset exceeding $5 * 10^6$ data, including nonpolar and polar molecules, radicals, long-chain molecules, and ions. These BWF transport properties calculated by the BWF potential have been compared against the Lennard-Jones transport properties as well as experimental viscosity, mass diffusivity, and thermal conductivity coefficients. It shows discrepancies of viscosity coefficients within 1% and 5% for nonpolar and polar molecules, respectively. Furthermore, this potential model is applied to study radicals, long-chain molecules, and ions, for which the experimental data is rarely accessed in high accuracy. It indicates significant prediction improvements of complex interactions between various particles. The new transport properties are also embedded into combustion simulations to predict the laminar flame speeds and the flame extinction limits of methane, dimethyl ether, and n-heptane at elevated pressures, confirming its predictivity and effectiveness.

1. Introduction

Real fluids, such as supercritical fluid, high-enthalpy fluid, and plasma, play an important role in propulsion and energy conversion scenarios: (i) supercritical spray, active cooling, and combustion in advanced combustion engines and rockets, (ii) thermal protection of hypersonic aircrafts and reentry of satellites, (iii) plasma-assisted propulsion, ignition, synthesis, and material treatment, etc. In such processes, intermolecular interactions are significantly amplified. For example, the supercritical combustion takes place when the fuel and the oxidizer interact at the supercritical phase at elevated pressures and temperatures. Due to the shorter molecular distance and faster collisions in the intense interactions of supercritical fluids, it provides a higher thermodynamic efficiency and lower emissions in advanced internal combustion engines and rockets [1–4]. Another example is plasma-assisted combustion and synthesis, where the highly non-equilibrium reactive flow is created in plasma with increased ionizations and excitations of molecules, radicals, and ions. These energetic species accelerate ignitions, combustions, and material synthesis in a non-equilibrium way under an intense intermolecular force field [5–7].

The real-fluid effects come from strong intermolecular interactions, manifesting in the compressibility, thermodynamic, and transport properties, which further affect combustion characteristics, such as the laminar flame speed and the flame extinction limit. Bai [8] computed the compressibility and thermodynamic properties of nonpolar and polar molecules by employing the Virial equation of state (EoS) [9] based on the Lennard-Jones potential [10] and the Stockmayer potential [11]. It is found that the predictions incorporating real-fluid effects significantly outperform the empirical Redlich-Kwong (RK) EoS [12] below 200 atm. Terashima and Koshi [13] also presented a real-fluid combustion model, and the results of one-dimensional propagating

* Corresponding authors.
E-mail addresses: h.zhao@pku.edu.cn (H. Zhao), tzhu@lps.ecnu.edu.cn (T. Zhu).

https://doi.org/10.1016/j.jaecs.2025.100342
Received 4 April 2025; Received in revised form 28 May 2025; Accepted 29 May 2025
Available online 14 June 2025

flames under a wide range of pressure conditions demonstrated that the real-fluid consideration offers a better prediction accuracy for the negative pressure dependence of the mass burning rate in the $H_2/O_2/Ar$ flame case compared to the ideal-gas model.

Accurate transport properties are also essential in the combustion modeling [14–16]. Brown [17] and Jasper [18] extensively reviewed the methods for estimating transport properties. For instance, Stallcop [19–22] and Wang [23–25] provided the collision cross sections and diffusion coefficients of binary collision systems, such as H/N_2 and H/Ar, using the first-principle method. Dagdigian [26–28] performed detailed calculations of the transport properties of H/CO, H/CO_2, and H_2O/H collision pairs using the quantum scattering method. Violi [29,30] used molecular dynamics simulations to determine the diffusion coefficients of long-chain alkanes and revealed the effect of the molecular configuration on the diffusion coefficients. Patidar [31] used the advanced Ab-initio method to provide potential energy surfaces and transport coefficients of a variety of high-energy organic molecules with four bath gases.

Presently, most of the calculations for transport properties above are based on the Lennard-Jones potential [10] and the Stockmayer potential [11] (hereafter both potentials are referred to as the LJ potential), which are used by CHEMKIN [32] and Cantera [33] simulations and have been the dominant force fields in the field of combustion. However, the LJ potential has some shortcomings. Jasper [34,35] studied the application of the LJ potential in the transport property calculations in detail. It was found that significant transport errors were introduced due to the isotropic approximation and the description of repulsive interaction. (i) The anisotropy, though negligible in small-scale systems such as H/N_2 and H_2/N_2, can exhibit a significant effect for the larger species such as $n\text{-}C_4H_{10}/N_2$ at lower temperatures, resulting in a 15% error in the diffusion coefficient computations. Violi [29,30] also emphasized the significance of the anisotropy on the transport properties, particularly for large molecules. (ii) Moreover, the incomplete description of the repulsive wall is a significant source of errors, introducing errors of up to 40% by using a steeper repulsive wall in the LJ potential than Buckingham (exp/6) potential [36]. Therefore, the LJ potential has good predictions for the simple nonpolar molecule systems, but is often unsatisfactory for long-chain molecules. In addition, the inert gas is required to be introduced as the bath gas when calculating the transport properties of polar molecules utilizing the LJ potential, whereas the mixing rules introduce extra errors [37]. For the above considerations, there is an urgent need to develop a new potential model with accurate and comprehensive descriptions of intermolecular interactions at high pressures.

In this study, we will develop a Boltzmann-weighted Full-dimensional (BWF) potential model for the real fluids. This model takes into account various intermolecular interactions including the repulsive, induction, dispersion, and electrostatic interactions. The anisotropy and temperature dependence of potential parameters are also considered by applying the Boltzmann weighting on all intermolecular orientations. Subsequently, we train the Boltzmann-weighted Full-dimensional potential parameters across nonpolar and polar molecules, radicals, long-chain molecules, and ions by the dataset from the high-level Symmetry-Adapted Perturbation Theory [38] calculations. Then, the Boltzmann-weighted Full-dimensional transport properties calculated by the BWF potential parameters are compared with the LJ transport properties in the literature and the National Institute of Standards and Technology (NIST) database [39]. Finally, we have embedded the new transport properties into combustion simulations, and calculated laminar flame speeds and flame extinction limits for various fuels, such as methane, dimethyl ether, and n-heptane.

2. Theory and method

2.1. Transport property calculation

The viscosity coefficient η, mass diffusivity coefficient D, and thermal conductivity coefficient λ are developed from the kinetic theory using classical mechanics of binary collisions as described by Hirschfelder [9] (Eqs. (1)–(3)). Potential parameters are used to calculate the transport properties of each species at different temperatures and pressures.

$$\eta = \frac{5}{16}\frac{\sqrt{\pi m k_B T}}{\pi\sigma^2\Omega^{(2,2)*}} \tag{1}$$

$$D = \frac{3}{16}\frac{\sqrt{\frac{2\pi k_B{}^3 T^3}{m}}}{p\pi\sigma^2\Omega^{(1,1)*}} \tag{2}$$

$$\lambda = \frac{\eta}{w}\left(f_{\text{trans}}C_{v,\text{trans}} + f_{\text{rot}}C_{v,\text{rot}} + f_{\text{vib}}C_{v,vib}\right) \tag{3}$$

where $k_B, m, T, w, \sigma,\ p, and\ \Omega^{(l,s)*}$ are the Boltzmann constant, mass of the molecule, temperature, molecular weight, molecule diameter, pressure, and the collision integral, respectively. And the individual species conductivities are composed of translational, rotational, and vibrational contributions (Eq. (4)).

$$\begin{aligned} f_{\text{trans}} &= \frac{5}{2}\left(1 - \frac{2}{\pi}\frac{C_{v,\text{rot}}}{C_{v,\text{trans}}}\frac{A}{B}\right), C_{v,\text{trans}} = 1.5R \\ f_{\text{rot}} &= \frac{\rho D}{\eta}\left(1 + \frac{2}{\pi}\frac{A}{B}\right), C_{v,\text{rot,nonlinear}} = 1.0R, C_{v,\text{rot,linear}} = 1.5R \\ f_{vib} &= \frac{\rho D}{\eta}, \quad C_{v,vib} = C_v - C_{v,\text{trans}} - C_{v,\text{rot}} \\ A &= \frac{5}{2} - \frac{\rho D}{\eta}, B = Z_{\text{rot}} + \frac{2}{\pi}\left(\frac{5}{3}\frac{C_{v,\text{rot}}}{R} + \frac{\rho D}{\eta}\right) \end{aligned} \tag{4}$$

where $C_{v,\text{rot}}, C_{v,\text{trans}}, C_{v,\text{vib}}$ are the rotational contribution, translational contribution, vibrational contribution to the molar specific heat of the species, respectively. And R, ρ, Z_{rot} are the universal gas constant, density, rotational relaxation collision number.

However, Hirschfelder et al. [9] pointed out that the transport properties calculated using the above formulas do not consider the pressure dependence. The transport properties are solely functions of temperature. Therefore, based on the Enskog theory [9] (Eqs. (5)–(8)), we computed the correction factors for the BWF model and the LJ model to obtain corrected transport coefficients over a wide range of temperatures and pressures.

$$\frac{\eta\tilde{V}}{\eta^0 b_0} = \frac{1}{y} + 0.8 + 0.761y \tag{5}$$

$$\frac{\lambda\tilde{V}}{\lambda^0 b_0} = \frac{1}{y} + 1.2 + 0.755y \tag{6}$$

$$\frac{pD}{(pD)^0}\frac{\tilde{V}}{b_0} = \frac{1}{y} + 1 \tag{7}$$

$$y = \frac{\tilde{V}}{RT}\left[T\left(\frac{\partial p}{\partial T}\right)_{\tilde{V}}\right] - 1 \tag{8}$$

The superscript of 0 indicates transport properties at atmospheric pressure. $\tilde{V}, p, b_0, y$ are the molar volume of species, pressure, gas volume constant ($b_0 = \frac{2}{3}\pi\tilde{N}\sigma^3$, $\tilde{N}$ is the Avogadro constant), and the correction factor from the partial derivation of the equation of state, respectively.

Here, we use the Virial coefficient equation of state and calculate the 2nd and 3rd virial coefficients from the BWF and the LJ potential models based on the statistical mechanics [9]. Then we obtain the Virial equation of states and the correction factors y for each species.

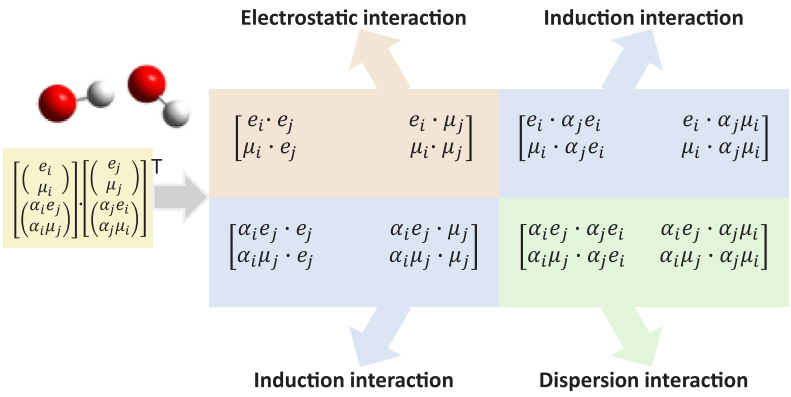

Fig. 1. The second-order tensor interaction space between molecules.

2.2. Potential model

In the field of the molecular dynamics, a profound comprehension of the intermolecular interaction is crucial for predicting the behavior of combustion systems. For simple nonpolar gases, which only involve the repulsive and dispersion interactions, simple potential models, such as the LJ potential, can give a good description. However, in more complex molecular systems, various types of interactions come into play.

To delve into the diverse interactions between molecules, we scrutinize their behavior based on the distance between the centers of particles. When two molecules are in close proximity, their electron clouds will overlap. According to the Pauli exclusion principle [40], two identical fermions cannot occupy the same quantum state, leading to the repulsive interaction. The intermolecular proximity repulsion is typically expressed in the form of $1/r^n$ or exp(b/r). In the field of combustion, we usually use the expression $1/r^{12}$ [17]. Conversely, when molecules are far apart, the dominance shifts to the interaction of their electric fields. The electric field of a molecule is divided into its intrinsic electric field and its polarized electric field induced by neighboring molecules. Based on the type of interacting electric field, we classify long-range interactions into the electrostatic, dispersion, and induction interactions, creating a second-order tensor interaction space as is illustrated in Fig. 1.

$$\varphi = \varphi_{repul} + \varphi_{elst} + \varphi_{indu} + \varphi_{disp} \tag{9}$$

We derived Boltzmann-weighted expressions (Eqs. S6–S8) for electrostatic, induction, and dispersion interactions [9]. Summing them up yields the complete interaction expression between molecules,

$$\begin{aligned}\bar{\varphi}(r) =& \bar{\varphi}_{repul} + \bar{\varphi}_{elst} + \bar{\varphi}_{indu} + \bar{\varphi}_{disp}\\ =& 4\varepsilon\left(\frac{\sigma}{r}\right)^{12}\\ &- \left[-\frac{e_i e_j}{r} + \frac{{e_i}^2{\mu_j}^2 + {e_j}^2{\mu_i}^2}{3k_BT\cdot r^4} + \frac{2{\mu_i}^2{\mu_j}^2}{3k_BT\cdot r^6}\right.\\ &+ \left(\frac{\alpha_i {e_j}^2}{2r^4} + \frac{\alpha_j {e_i}^2}{2r^4}\right) + \left(\frac{\alpha_i {\mu_j}^2}{r^6} + \frac{\alpha_j {\mu_i}^2}{r^6}\right)\\ &\left.+ \frac{1.5\alpha_i\alpha_j}{r^6}\left(\frac{I_i I_j}{I_i + I_j}\right)\right]\end{aligned} \tag{10}$$

where, $\varepsilon, \sigma, r, e, \mu, \alpha, I$ are the potential well, molecular diameter, distance between two molecules, charge, dipole moment, polarizability, first ionization potential, respectively. The i or j in the subscript represents the properties of the molecule i or j. Most of existing potential models determine the potential parameters of pure gas by introducing bath gas and employing the mixing rule to model, which often causes uncertainty of parameters. Thus, we directly calculate potential parameters of the pure gas.

$$\alpha_i = \alpha_j = \alpha, e_i = e_j = e, \mu_i = \mu_j = \mu, I_i = I_j = I \tag{11}$$

Then Eq. (10) is simplified as follows,

$$\begin{aligned}\bar{\varphi}(r) =& 4\varepsilon\left(\frac{\sigma}{r}\right)^{12}\\ &- \left[-\frac{e^2}{r} + \frac{2e^2\mu^2}{3k_BT\cdot r^4} + \frac{2\mu^4}{3k_BT\cdot r^6}\right.\\ &+ \frac{\alpha e^2}{r^4} + \frac{2\alpha\mu^2}{r^6}\\ &\left.+ \frac{0.75\alpha^2 I}{r^6}\right]\end{aligned} \tag{12}$$

$$\begin{aligned}\bar{\varphi}(r) =& 4\varepsilon\left[\left(\frac{\sigma}{r}\right)^{12} + \frac{e^2}{4\varepsilon\sigma}\frac{\sigma}{r}\right.\\ &- \left(\frac{2e^2\mu^2}{3k_BT\cdot 4\varepsilon\sigma^4} + \frac{\alpha e^2}{4\varepsilon\sigma^4}\right)\left(\frac{\sigma}{r}\right)^4\\ &\left.- \left(\frac{2\mu^4}{3k_BT\cdot 4\varepsilon\sigma^6} + \frac{2\alpha\mu^2}{4\varepsilon\sigma^6} + \frac{0.75\alpha^2 I}{4\varepsilon\sigma^6}\right)\left(\frac{\sigma}{r}\right)^6\right]\end{aligned} \tag{13}$$

Next, we introduce a shape correction based on Eq. (13) according [41],

$$\begin{aligned}\bar{\varphi}(r) =& 4\varepsilon\left[(1+2D_s)\left(\frac{\sigma}{r}\right)^{12} + \frac{e^2}{4\varepsilon\sigma}\frac{\sigma}{r}\right.\\ &- \left(\frac{2e^2\mu^2}{3k_BT\cdot 4\varepsilon\sigma^4} + \frac{\alpha e^2}{4\varepsilon\sigma^4}\right)\left(\frac{\sigma}{r}\right)^4\\ &\left.- \left(\frac{2\mu^4}{3k_BT\cdot 4\varepsilon\sigma^6} + \frac{2\alpha\mu^2}{4\varepsilon\sigma^6} + \frac{0.75\alpha^2 I}{4\varepsilon\sigma^6}\right)\left(\frac{\sigma}{r}\right)^6\right]\end{aligned} \tag{14}$$

The shape correction factor is,

$$D_s = A\left[1 - \left(\frac{L_2}{L_1}\right)\right] \tag{15}$$

where L_1 and L_2 are the length and width of the main chain of the molecule respectively, and A is 0.50 for rodlike and −0.25 for platelike molecules.

The accuracy of a potential model depends heavily on the computed potential energy surfaces, in addition to the chosen functional form. Nowadays, many software packages, such as Gaussian and ORCA, can apply the Basis Set Superposition Error (BSSE) [42] correction to calculate the potential energy surface between two molecules. However, this method requires significantly more computational efforts, typically more than twice the time of uncorrected calculations [43]. Thus, researchers proposed the Symmetry-Adapted Perturbation Theory (SAPT) [38], which provided a direct method for calculating intermolecular potential energies. By applying perturbation to a system, intermolecular interactions can be evaluated without the BSSE correction. Several programs can perform SAPT calculations, among which the PSI4 software [44] stands out as a suitable choice. PSI4 is not only open-source and efficient, but also provides SAPT2+3 level accuracy.

Therefore, in this paper, we use PSI4 to calculate the potential energy surfaces.

In PSI4, the calculation accuracy increases with the level of perturbation considered: SAPT0 < SAPT2 < SAPT2+ < SAPT2+(3) < SAPT2+3. At the same time, the choice of basis set also affects the accuracy. Three combinations are recommended for optimal accuracy, in increasing order [45]: sSAPT0/jun-cc-pVDZ < SAPT2+/aug-cc-pVDZ < SAPT2+(3)δMP2/aug-cc-pVTZ.

Lu [46] demonstrated that the SAPT2+(3)δMP2/aug-cc-pVTZ combination yields accurate intermolecular interaction predictions, with relative errors of only 3% compared to the high-accuracy CCSD(T)/jun-cc-pVTZ benchmark and absolute errors below 0.1 kcal/mol, while requiring only one-tenth of the computational time. Therefore, in this work, the SAPT2+(3)δMP2/aug-cc-pVTZ level is employed to calculate the potential energy surfaces between molecular pairs. However, due to the open-shell structures of free radicals and the large size of long-chain molecules, these systems are restricted to the SAPT0/jun-cc-pVDZ and sSAPT0/jun-cc-pVDZ levels, respectively. For free radicals, we use the SAPT0 approach based on the unrestricted Hartree–Fock (UHF) reference, which is the only open-shell SAPT variant currently implemented in PSI4. At the same time, we set the spin multiplicity and obtain the intermolecular interaction approximation for free radical systems.

In addition, in order to construct the full-dimensional potential energy surfaces, we performed a direction-dependence test. As is shown in Fig. S1, the potential energy surface converges at 432 orientations. Under the above computational settings, we computed potential energy surfaces of various species at 432 orientations using PSI4. These direction-dependent potential energy curves were then combined by Boltzmann weighting to generate a single effective potential energy curve. This Boltzmann-weighted full-dimensional potential energy curve captured both the anisotropy and temperature dependence of intermolecular interactions and was subsequently parameterized using the BWF potential model. Using this approach, we derived a set of BWF potential parameters for polar and nonpolar molecules, free radicals, long-chain molecules, and ions. These parameters can be directly incorporated into the transport input files for CHEMKIN, Cantera, and other simulation platforms, as are presented in Tables S1-S5.

3. Results and discussion

3.1. Transport properties

3.1.1. Common small molecule

Before delving into the study of complex molecules, the BWF potential model is verified through transport property predictions, such as the viscosity, mass diffusivity, and thermal conductivity coefficients of small molecules against the TRANLIB library [47], potential parameters in the literature, and the NIST library [39]. It is noted that most transport coefficients in present combustion simulations are accomplished from the TRANLIB library and embedded into CHEMKIN [32] and Cantera [33] numerical simulations [17].

For nonpolar molecules such as H_2, N_2, and O_2, we calculate viscosity, mass diffusivity, and thermal conductivity coefficients for each nonpolar gas across a wide range (300-2400 K) by incorporating the potential parameters into Eqs. (1)–(3). Fig. 2 exhibits the viscosity coefficients with temperature. The BWF and the TRANLIB (LJ) viscosity coefficients possess errors less than 1% from experimental values for H_2, N_2, and O_2, exhibiting excellent predictabilities. While the Gorbachev (LJ) model creates a relative error of 9.5% for H_2, the Cuadros (LJ) and Mamedov (LJ) models maintain errors of 6% for N_2. Most LJ or exp/6 potential models in the literature fail to accurately describe intermolecular interactions of O_2 due to its unique open-shell energy structure. For instance, the Hobbs (exp/6) model displays a relative error of 23%. Similarly, as are shown in Figs. S4 and S5, the BWF potential model shows the best consistency with the TRANLIB library and experimental values for mass diffusivity and thermal conductivity coefficients.

For polar molecules such as H_2O, NH_3, and H_2S, the BWF and the TRANLIB (LJ) viscosity coefficients exhibit errors within 5% from experimental values in Fig. 2. Unfortunately, other LJ or exp/6 potential models in the literature remain larger uncertainties. For example, the Somuncu (LJ) model shows relative errors of 10% for H_2O and 28.3% for NH_3. Moreover, for the mass diffusivity and thermal conductivity coefficients of polar gases, the BWF potential model also reveals the highest accuracy with experimental values, as are shown in Figs. S4 and S5.

Unfortunately, in most cases, the pressure dependence is not considered in the transport property computations, while it becomes non-negligible for real fluids, such as supercritical fluid at high pressures. Therefore, for real-fluid computations, we have corrected the pressure dependences of viscosity (Fig. 3), mass diffusivity (Fig. S6), and thermal conductivity (Fig. S7) coefficients based on the Enskog theory [9] (Eqs. (5)–(8)). It shows that the corrected transport coefficients exhibit significant pressure dependences across a wide pressure range of 1-600 atm. For nonpolar gases, such as H_2, N_2, and O_2, the relative errors of the BWF and the TRANLIB (LJ) viscosity coefficients are around 1%–3%. However, the relative errors of the Mamedov (LJ) model reach 6% for H_2 and N_2, and the Hobbs (exp/6) viscosity coefficients for O_2 reach an error of 22%, which is beyond the acceptable prediction error of 5% [17].

As is shown in Figs. 3 (d)–(f), for polar molecules, such as H_2O, NH_3, and H_2S, even though these LJ potential models account for the electrostatic interaction between dipole moments (the Stockmayer potential), their predictive ability remains inadequate. For NH_3, the prediction error of the BWF viscosity coefficients is around 3%, while the error of the TRANLIB (LJ) model reaches 15.6% at 250 atm, and other LJ potentials exhibit even higher errors. Furthermore, several LJ potentials in Figs. 3 (d) and (e) significantly diverge beyond 250 atm. Therefore, the BWF model exhibits a higher prediction accuracy for nonpolar and polar molecules than various LJ models in the literature as the former takes various intermolecular interactions in account comprehensively.

3.1.2. Radicals, long-chain molecules, and ions

It is noted that the transport coefficient data in the TRANLIB library is mainly fitted from experimental measurements [17]. Therefore, it agrees well with the experimental transport coefficients of nonpolar and polar molecules. The successful agreement between our theoretical BWF potential model and the TRANLIB library and experimental values in the broad range of temperatures and pressures (300-2400 K and 1-600 atm), confirms its applicability for transport property predictions. The BWF potential parameters of nonpolar and polar gases are provided in the Tables S1 and S2. Unfortunately, for radicals, long-chain molecules, and ions, where the experimental data is rarely accessed, the TRANLIB library loses its fitting accuracy.

Radicals own the high reactivity, short life time, and large polarity, resulting in difficulties in experimental measurements and rigorous calculations. As are shown in Figs. 4 (a) and (b), the energy potential surfaces of CH_3 and C_2H_5 are plotted using the TRANLIB (LJ) and the BWF potential parameters, and compared with the theoretical trajectory from high-level quantum chemistry computations. It is evident that the LJ potential model cannot accurately describe the potential energy surfaces, especially the repulsive walls [34]. In contrast, the BWF potential model, after considering comprehensive intermolecular interactions and introducing more potential parameters, effectively improves the repulsive walls of the potential surfaces, aligning closely with the theoretical energy-potential trajectory. Since there are a large number of radicals in the combustion system, it is particularly important to improve their transport properties. We have calculated the potential parameters of a large number of radicals, CH, CH_2, CH_3, C_2H_3, C_2H_5, CHO, H, and other radicals, as are shown in Table S3.

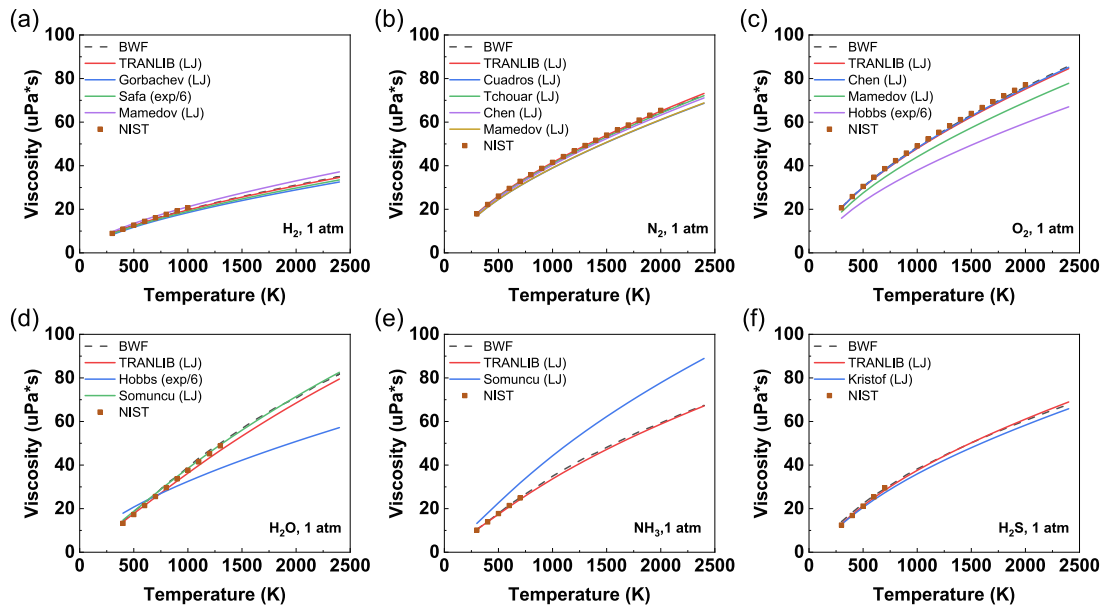

Fig. 2. Viscosity coefficients of nonpolar and polar gases at different temperatures (BWF: the Boltzmann-weighted Full-dimensional Potential, LJ: the Lennard–Jones potential, exp/6: the Buckingham potential [36]) (a) H_2: Gorbachev [48], Safa [49], Mamedov [50], NIST [39]; (b) N_2: Cuadros [51], Tchouar [52], Chen [53], Mamedov [50], NIST [39]; (c) O_2: Chen [53], Mamedov [50], Hobbs [54], NIST [39]; (d) H_2O: Hobbs [54], Somuncu [55], NIST [39]; (e) NH_3: Somuncu [55], NIST [39]; (f) H_2S: Kristof [56], NIST [39].

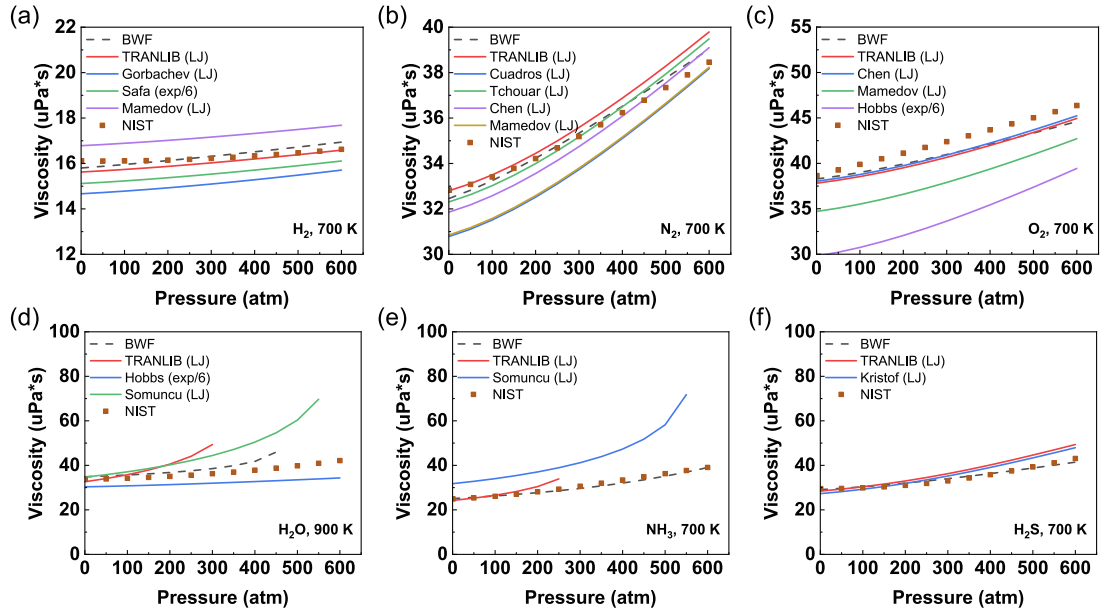

Fig. 3. Viscosity coefficients of nonpolar and polar gases at different pressures (BWF: the Boltzmann-weighted Full-dimensional Potential, LJ: the Lennard–Jones potential, exp/6: the Buckingham potential [36]) (a) H_2: Gorbachev [48], Safa [49], Mamedov [50], NIST [39]; (b) N_2: Cuadros [51], Tchouar [52], Chen [53], Mamedov [50], NIST [39]; (c) O_2: Chen [53], Mamedov [50], Hobbs [54], NIST [39]; (d) H_2O: Hobbs [54], Somuncu [55], NIST [39]; (e) NH_3: Somuncu [55], NIST [39]; (f) H_2S: Kristof [56], NIST [39].

As the main components of fuels, the transport properties of long-chain molecules are pivotal for combustion simulations. Due to their long-chain structure, treating these molecules as simple point particles introduces significant errors into transport properties [29,30,34]. Therefore, we introduce a shape correction based on Eqs. (13) and (14) in the section of Materials and Methods. As are shown in Figs. 4 (c) and (d), the potential energy surfaces of the TRANLIB (LJ) and the BWF potential model show significant differences. The LJ potential surface without shape correction deviates significantly from the Symmetry-Adapted Perturbation Theory calculations, and seriously underestimates the diameter of the molecules, estimating only the propane molecular diameter of 4.81 Åand the pentane molecular diameter of 5.596 Å. Therefore, considering the internal configuration of long-chain molecules and the shape correction is crucial for the accurate description of the interactions between long-chain molecules. Using the corrected potential model, we trained the dataset of long-chain molecules and derived the corresponding potential parameters, as are shown in Table S4.

Traditional potential models, such as the LJ potential model, often overlook electrostatic and induction interactions and only handle the simplest uncharged molecules. However, with the continuous development of combustion research, such as the plasma-assisted combustion, how to deal with the charged particles in the combustion system has

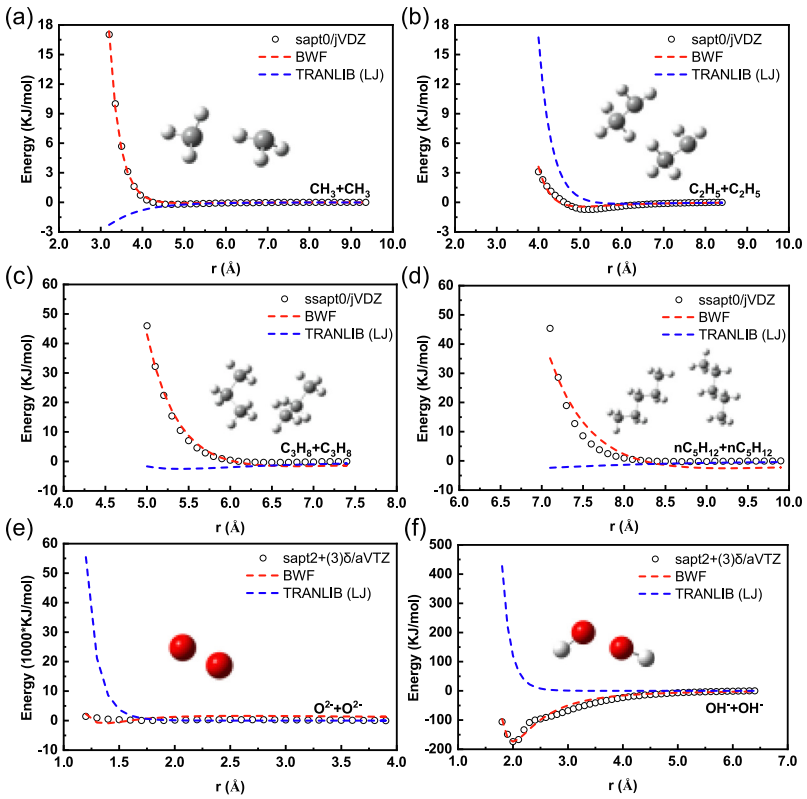

Fig. 4. The Boltzmann-weighted Full-dimensional potential energy surfaces for radicals, long-chain molecules, and ions (o: the SAPT computations, sapt0/jVDZ: SAPT0/jun-cc-pVDZ combination in PSI4 software, ssapt0/jVDZ: sSAPT0/jun-cc-pVDZ combination in PSI4 software, sapt2+(3)δ/aVTZ: SAPT2+(3)δMP2/aug-cc-pVTZ combination in PSI4 software) (a) CH_3; (b) C_2H_5; (c) C_3H_8; (d) nC_5H_{12}; (e) O^{2-}; (f) OH^-.

become an important topic to be concerned about. In addition to the basic repulsive and dispersion interactions, the BWF potential model also takes into account electrostatic and induction interactions. It can describe the interaction of various particles, including uncharged and charged particles. As are shown in Figs. 4 (e) and (f), the BWF potential model can accurately reproduce the interaction between charged particles, addressing for the shortcoming that the traditional LJ potential model cannot deal with charged particles. The potential parameters of OH^- and O^{2-} are shown in Table S5.

3.2. Combustion characteristics

The model validation above has successfully confirmed that in a wide range of temperatures and pressures (300-2400 K and 1-600 atm), the BWF potential model exhibits comprehensive and accurate predictions of transport properties of nonpolar and polar molecules, radicals, long-chain molecules, and ions simultaneously, while other models in the literature lacks the similar versatility and accuracy. Therefore, the BWF potential model is applied in the real-fluid simulation away from the ideal-gas equilibrium, such as supercritical fluid, high-enthalpy fluid, plasma interactions.

Supercritical combustion, known for its high thermodynamic efficiency and low emissions, has gained significant attention, particularly in advanced engines and gas turbines. Notably, the Raptor engine of the SpaceX Starship operated in the supercritical combustion region using a CH_4/O_2 mixture at pressures exceeding 300 atm [57]. However, a number of problems, such as engine misfires and malfunctions (3 Raptor engines misfired during the first launch of the Starship), flame instability was found in the Raptor engine operation, implying that our current research on the supercritical combustion is still insufficient, and it is necessary to carefully consider the real-fluid behavior in extreme combustion conditions like supercritical combustion. Therefore, this work investigates combustion characteristics such as the laminar flame speed and the flame extinction limit of methane at atmospheric and high pressures. In addition, to explore the influence of real-fluid effects on fuels with different carbon-chain lengths, we have also conducted insightful studies on dimethyl ether (DME) and n-heptane.

The laminar flame speeds and the flame extinction limits of fuels are calculated using the PREMIX and the OPPDIF modules of the CHEMKIN package, respectively. Various detailed and reduced chemical kinetic models are evaluated against the experimental flame laminar speeds and extinction limits. The GRI3.0 mechanism [58], the HPmech-1.3 mechanism [59], and the simplified n-heptane mechanism [60] by the PFA method [61] are employed to simulate and predict methane, dimethyl ether, and n-heptane fuels, respectively.

3.2.1. The flame extinction limit

Three Raptor engines of the Starship misfired during the first launch of the interplanetary spacecraft, and our understanding of the flame extinction characteristics is still incomplete. We have investigated the flame extinction limits including methane, DME, and n-heptane, as are shown in Figs. 5–7, respectively. The axial velocity gradient at the oxidizer side is defined as a global strain rate [62], $a_{ext} = 2U_o/L[1 + (U_f/U_o)(\rho_f/\rho_o)^{1/2}]$, where U_o and U_f are the flow velocities of oxidizer and fuel streams, and ρ_o and ρ_f the densities of oxidizer and fuel streams, respectively. Compared with the experimental data, the predictions of the BWF and the TRANLIB (LJ) extinction limits for methane are close to each other, showing relative prediction deviations of 5%–15% with experimental measurements. However, for the long-chain molecules such as n-heptane, the BWF potential model exhibits the prediction error level of 10% from the experimental data, while the TRANLIB (LJ) model possesses a significant uncertainty above 50% from experiments. As the flame extinction is highly relevant to transport properties of molecules through the extinction strain rate [15, 25], the accurate computations of transport properties using the BWF potential model show a significant improvement in flame extinction

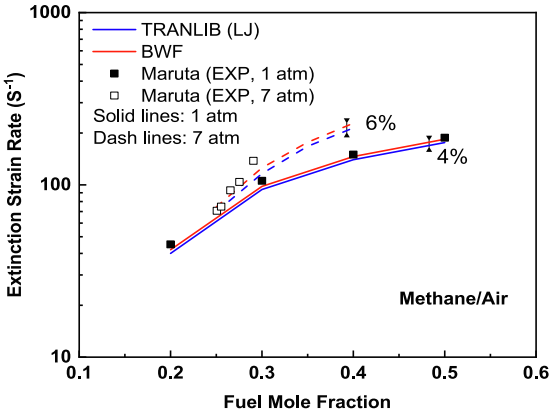

Fig. 5. The flame extinction limits of the methane /air at an initial fuel temperature of 550 K, an initial air temperature of 300 K, and initial pressures of 1 and 7 atm with comparisons to the experimental data: Maruta [63].

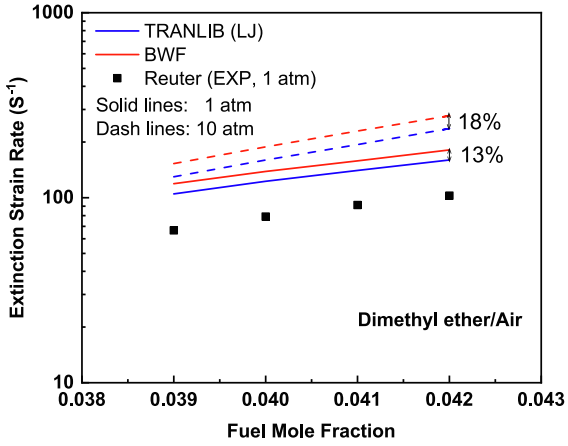

Fig. 6. The flame extinction limits of the dimethyl ether /air at an initial fuel temperature of 550 K, an initial air temperature of 300 K, and initial pressures of 1 and 10 atm with comparisons to the experimental data: Reuter [64].

predictions than LJ models, especially for long-chain molecules where shape corrections are not considered in LJ models in the literature. This underscores the importance of considering the molecular configuration and anisotropy to enhance the prediction accuracy of transport and combustion properties. In addition, the BWF potential model may makes larger difference at higher pressures for flame extinction predictions, while unfortunately, higher pressure data of flame extinction limits are not available in the literature for the model validation.

3.2.2. The laminar flame speed

Fig. 8 depicts the laminar flame speed versus the equivalent ratio for the methane/air mixture at 1 and 10 atm, and the methane/oxygen mixture at 300 atm. It shows that the predicted laminar flame speeds using the BWF and TRANLIB (LJ) method closely match the experimental data, with relative errors around 5% at 1 and 10 atm. Notably, the BWF potential model aligns slightly better with experimental data at 10 atm than the TRANLIB (LJ) method. While at 300 atm, the prediction discrepancy between two models was amplified. Moreover, the laminar flame speeds of DME and n-heptane are also compared in Figs. 9 and 10, the BWF laminar flame speed is in better agreement with the experimental data than the TRANLIB (LJ) model by up to 10% at both 1 and 10 atm. Therefore, it indicates a high accuracy of the BWF method for predicting laminar flame speeds, especially for long-chain fuels.

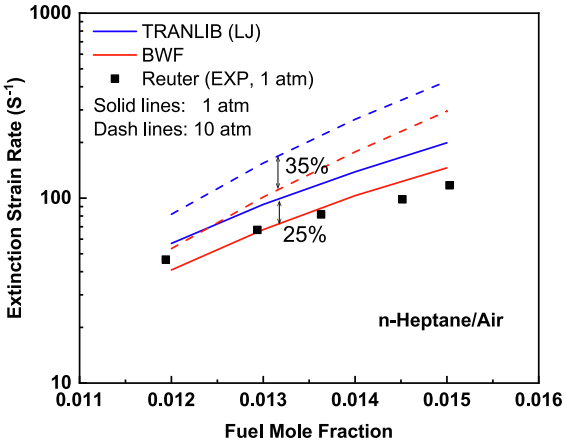

Fig. 7. The flame extinction limits of the n-heptane/air at an initial fuel temperature of 550 K, an initial air temperature of 300 K, and initial pressures of 1 and 10 atm with comparisons to the experimental data: Reuter [65].

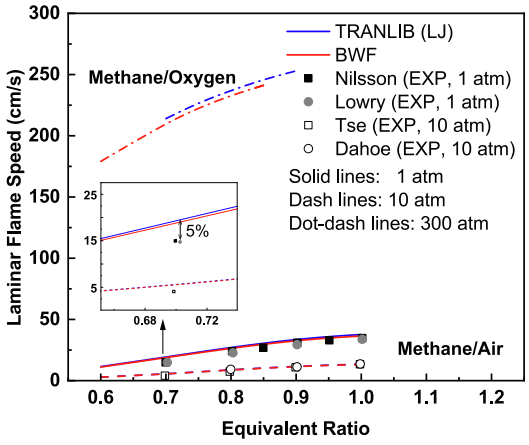

Fig. 8. The laminar flame speeds of methane at an initial temperature of 300 K and pressures of 1 atm (methane/air), 10 atm (methane/air), and 300 atm (methane/oxygen) with comparisons to the experimental data: Nilsson [66], Lowry [67], Tse [68], Dahoe [69].

It is seen that the real-fluid potential model plays a larger impact on correcting the flame extinction limit than the laminar flame speed due to a higher transport relevance. Unfortunately, there is a lacking of experimental data for the measurement of laminar flame speeds and extinction limits above 50 atm to validate the BWF model at high pressures.

4. Conclusion

Numerical modeling stands as a pivotal instrument for in-depth study of extreme combustion conditions such as the supercritical combustion. Our research focuses on elucidating transport properties, particularly the mass diffusivity, viscosity, and thermal conductivity, which are key factors influencing on combustion simulations. Intermolecular interactions need to be considered in transport modeling, especially in cases where the real-fluid effects are significant. To meet this requirement, we construct a second-order tensor interaction space, the Boltzmann-weighted Full-dimensional potential model, which is adept at accommodating a wide variety of species, including nonpolar and polar gases, radicals, long-chain alkanes, and ionic species. The model effectively captures diverse intermolecular interactions, providing key potential parameters, such as the potential well, molecular diameter, dipole moment, and polarizability. No extra errors are introduced to

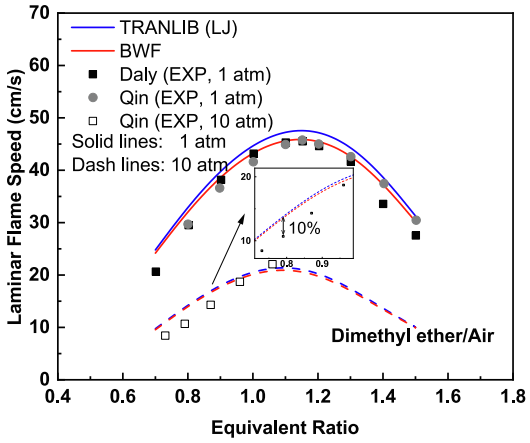

Fig. 9. The laminar flame speeds of the dimethyl ether/air at an initial temperature of 300 K and pressures of 1 and 10 atm with comparisons to the experimental data: Daly [70], Qin (1 atm) [71], Qin (10 atm) [71].

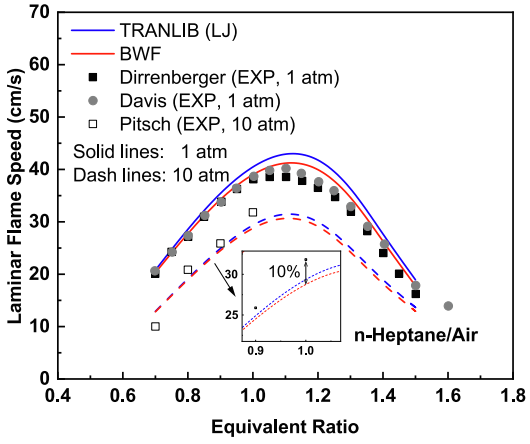

Fig. 10. The laminar flame speeds of the n-heptane/air at 300 K and 1 atm, 373 K and 10 atm with comparisons to the experimental data: Dirrenberger [72], Davis [73], Pitsch [74].

potential parameters by the mixing rules and bath gases. Moreover, the BWF potential model contains more parameters and describes the potential energy surface more accurately, effectively improving the problem that LJ model over-steeply predicts the repulsive walls. On this basis, its versatility extends to incorporating anisotropy and temperature dependence in potential parameters through Boltzmann weighting across various spatial orientations.

We conduct the high-level Symmetry-Adapted Perturbation Theory calculations using the PSI4 software, yielding a rich array of potential energy surface datasets. Through careful training on the dataset exceeding $5 * 10^6$ data, we successfully determine the Boltzmann-weighted Full-dimensional potential parameters for the common nonpolar and polar gases, radicals, long-chain alkanes, and ions. Then, we use the BWF potential parameters to provide the transport coefficients over a wide range of temperatures and pressures (300-2400 K and 1-600 atm). These BWF transport properties are compared with the LJ transport properties in the literature and experimental measurements. Encouragingly, the relative errors of the BWF transport properties hover around 1% for nonpolar gases and about 5% for polar molecules, which is within the acceptable error range of 5%. Expanding the potential to radicals, long-chain molecules, and ions, the BWF model accurately reproduces the complex interactions between various particles. It effectively addresses limitations of the LJ model, including the improper description of repulsive walls, the under-prediction of the diameters of long-chain molecules, and the unavailability of charged particles. Subsequently, we integrate the model into the combustion simulations to calculate laminar flame speeds and flame extinction limits for methane, dimethyl ether, and n-heptane at high and low pressures. The results confirm that the BWF model accurately predicts the combustion characteristics under various complex operating conditions. Notably, for long-chain alkane n-heptane, the BWF model can accurately improve the prediction of flame extinction limits, and differs by up to 35% from the LJ model between 1-10 atm.

In conclusion, this work marks a significant advance in real-fluid modeling. The development of the Boltzmann-weighted Full-dimensional potential model has successfully obtained and validated a variety of potential parameters, which can be used directly as transport input files for combustion simulation software, such as CHEMKIN and Cantera. Besides, a series of transport properties and combustion characteristics of fuels are obtained, which provides strong supports for the further advancements in the field of combustion.

CRediT authorship contribution statement

Xin Zhang: Software, Methodology, Conceptualization. **Junfeng Bai:** Software, Methodology, Data curation. **Bowen Liu:** Software, Investigation. **Tong Zhu:** Validation, Supervision. **Hao Zhao:** Validation, Supervision, Conceptualization.

Declaration of competing interest

The authors declare that they have no known competing financial interests or personal relationships that could have appeared to influence the work reported in this paper.

Acknowledgments

This work was supported by the National Natural Science Foundation of China (No. 22361132538, No. 22350710788) and the Fund of Ministry of Education (No. 8091B032244).

Appendix A. Supplementary data

Supplementary material related to this article can be found online at https://doi.org/10.1016/j.jaecs.2025.100342.

Data availability

Data will be made available on request.

References

[1] Gokulakrishnan P, Shao J, Klassen MS, Davidson DF, Hanson RK. NOx formation from ammonia, and its effects on oxy-combustion of hydrocarbon fuels under supercritical-CO2 conditions. Appl Energy Combust Sci 2023;13:100110.
[2] Sabatino FD, Connolly BJ, Pryor OM, White SH. Perspectives on oxy-fuel combustion for supercritical CO2 direct-fired power cycle. Appl Energy Combust Sci 2024;20:100297.
[3] Zhao H, Fu J, Haas FM, Ju Y. Effect of prompt dissociation of formyl radical on 1,3,5-trioxane and CH2o laminar flame speeds with CO2 dilution at elevated pressure. Combust Flame 2017;183:253–60.
[4] Zhao H, Yan C, Zhang T, Ma G, Souza MJ, Zhou C-w, et al. Studies of high-pressure n-butane oxidation with CO2 dilution up to 100 atm using a supercritical-pressure jet-stirred reactor. Proc Combust Inst 2021;38:279–87.
[5] Chen H, Zhang R, Liao H, Liu Z, Li Z, Zhang F, et al. Plasma-assisted low-temperature oxidation of n-butane: A synchrotron photoionization mass spectrometry and kinetic modeling study. Appl Energy Combust Sci 2023;14:100134.
[6] Guerra-Garcia C, Pavan CA. The backward problem in plasma-assisted combustion: experiments of nanosecond pulsed discharges driven by flames. Appl Energy Combust Sci 2023;15:100155.
[7] Ju Y, Lefkowitz JK, Reuter CB, Won SH, Yang X, Yang S, et al. Plasma assisted low temperature combustion. Plasma Chem Plasma Process 2016;36:85–105.

[8] Bai J, Zhang P, Zhou C-W, Zhao H. Theoretical studies of real-fluid oxidation of hydrogen under supercritical conditions by using the virial equation of state. Combust Flame 2022;243:111945.
[9] Hirschfelder J, Curtiss C, Bird R. Molecular Theory of Gases and Liquids. 2nd ed. New York, NY: John Wiley and Sons, Inc.; 1964.
[10] Lennard-Jones JE. On the determination of molecular fields. —II. from the equation of state of a gas. Proc R. Soc Lond A 1924;106:463–77.
[11] Stockmayer WH. Second virial coefficients of polar gases. J Chem Phys 1941;9:398–402.
[12] Redlich O, Kwong J. On the thermodynamics of solutions. V. An equation of state. Fugacities of gaseous solutions. Chem Rev 1949;44:233–44.
[13] Terashima H, Koshi M. Prediction of propagating flames under high-pressure conditions with real-fluid combustion modeling. Proc Combust Inst 2023;39:1823–31.
[14] Brown NJ, Revzan KL. Comparative sensitivity analysis of transport properties and reaction rate coefficients. Int J Chem Kinet 2005;37:538–53.
[15] Dong Y, Holley AT, Andac MG, Egolfopoulos FN, Davis SG, Middha P, et al. Extinction of premixed H2/Air flames: chemical kinetics and molecular diffusion effects. Combust Flame 2005;142:374–87.
[16] Esposito G, Chelliah H. Effect of binary diffusion and chemical kinetic parameter uncertainties in simulations of premixed and non-premixed laminar hydrogen flames. Combust Flame 2012;159:3522–9.
[17] Brown NJ, Bastien LA, Price PN. Transport properties for combustion modeling. Prog Energ Combust 2011;37:565–82.
[18] Miller JA, Sivaramakrishnan R, Tao Y, Goldsmith CF, Burke MP, Jasper AW, et al. Combustion chemistry in the twenty-first century: developing theory-informed chemical kinetics models. Prog Energ Combust 2021;83:100886.
[19] Stallcop JR, Partridge H, Walch SP, Levin E. H–N2 interaction energies, transport cross sections, and collision integrals. J Chem Phys 1992;97:3431–6.
[20] Stallcop JR, Partridge H, Levin E. H-H2 collision integrals and transport coefficients. Chem Phys Lett 1996;254:25–31.
[21] Stallcop JR, Levin E, Partridge H. Transport properties of hydrogen. J Thermophys Heat Tr 1998;12:514–9.
[22] Partridge H, Stallcop JR, Levin E. Potential energy curves and transport properties for the interaction of he with other ground-state atoms. J Chem Phys 2001;115:6471–88.
[23] Middha P, Yang B, Wang H. A first-principle calculation of the binary diffusion coefficients pertinent to kinetic modeling of hydrogen/oxygen/helium flames. Proc Combust Inst 2002;29:1361–9.
[24] Middha P, Wang H. First-principle calculation for the high-temperature diffusion coefficients of small pairs: The H–Ar Case. Combust Theor Model 2005;9:353–63.
[25] Liu C, Zhao R, Xu R, Egolfopoulos FN, Wang H. Binary diffusion coefficients and non-premixed flames extinction of long-chain alkanes. Proc Combust Inst 2017;36:1523–30.
[26] Dagdigian PJ, Alexander MH. Exact quantum scattering calculations of transport properties for the H2O–H system. J Chem Phys 2013;139:194309.
[27] Dagdigian PJ. Accurate transport properties for H–CO and H–CO2. J Chem Phys 2015;143:054303.
[28] Dagdigian PJ. Combustion simulations with accurate transport properties for reactive intermediates. Combust Flame 2015;162:2480–6.
[29] Chae K, Elvati P, Violi A. Effect of molecular configuration on binary diffusion coefficients of linear alkanes. J Phys Chem B 2011;115:500–6.
[30] Chae K, Violi A. Mutual diffusion coefficients of heptane isomers in nitrogen: A molecular dynamics study. J Chem Phys 2011;134:044537.
[31] Patidar L, Khichar M, Thynell ST. Intermolecular potential parameters for transport property modeling of energetic organic molecules. Combust Flame 2019;200:232–41.
[32] Kee R, Miller J, Jefferson T. CHEMKIN: A General-Purpose, Problem-Independent, Transportable, FORTRAN Chemical Kinetics Code Package. Technical Report SAND80-8003, Sandia National Laboratories; 1980.
[33] Goodwin D, Moffat H, Schoegl I, Speth R, Weber B. Cantera: An object-oriented software toolkit for chemical kinetics and thermodynamics and and transport processes. 2023, http://dx.doi.org/10.5281/zenodo.8137090, Version 3.0.0 https://www.cantera.org.
[34] Jasper AW, Kamarchik E, Miller JA, Klippenstein SJ. First-principles binary diffusion coefficients for h, H2, and four normal alkanes + N2. J Chem Phys 2014;141:124313.
[35] Jasper AW, Miller JA. Lennard–Jones parameters for combustion and chemical kinetics modeling from full-dimensional intermolecular potentials. Combust Flame 2014;161:101–10.
[36] Buckingham RA. The classical equation of state of gaseous helium, neon and argon. Proc R. Soc Lond A 1938;168:264–83.
[37] Bastien LAJ, Price PN, Brown NJ. Intermolecular potential parameters and combining rules determined from viscosity data. Int J Chem Kinet 2010;42:713–23.
[38] Jeziorski B, Moszynski R, Szalewicz K. Perturbation theory approach to intermolecular potential energy surfaces of van der waals complexes. Chem Rev 1994;94:1887–930.
[39] Linstrom PJ, Mallard WG. NIST chemistry WebBook. In: NIST standard reference database number 69. 2024, 20899. http://dx.doi.org/10.18434/T4D303, retrieved May 14.
[40] Pauli W. Pauli exclusion principle. Naturwiss 1924;12:741.
[41] Johnson JR, Eubank PT. Intermolecular interactions of highly polar gases. Ind Eng Chem Fund 1973;12:156–65.
[42] Gutowski M, Van Lenthe J, Verbeek J, Van Duijneveldt F, Chałasinski G. The basis set superposition error in correlated electronic structure calculations. Chem Phys Lett 1986;124:370–5.
[43] Burns LA, Marshall MS, Sherrill CD. Comparing counterpoise-corrected, uncorrected, and averaged binding energies for benchmarking noncovalent interactions. J Chem Theory Comput 2014;10:49–57.
[44] Turney JM, et al. An open-source ab initio electronic structure program. WIREs Comput Mol Sci 2012;2:556.
[45] Parker TM, Burns LA, Parrish RM, Ryno AG, Sherrill CD. Levels of symmetry adapted perturbation theory (SAPT). I. efficiency and performance for interaction energies. J Chem Phys 2014;140:094106.
[46] Emamian S, Lu T, Kruse H, Emamian H. Exploring nature and predicting strength of hydrogen bonds: a correlation analysis between atoms-in-molecules descriptors, binding energies, and energy components of symmetry-adapted perturbation theory. J Comput Chem 2019;40:2868–81.
[47] Kee RJ, Dixon-Lewis G, Warnatz J, Coltrin ME, Miller JA. A Fortran Computer Code Package for the Evaluation of Gas-Phase, Multicomponent Transport Properties. Technical Report SAND-86-8246, Sandia National Laboratories; 1986.
[48] Gorbachev YE, Zatevakhin MA, Krzhizhanovskaya VV, Shveigert VA. Special features of the growth of hydrogenated amorphous silicon in PECVD reactors. Tech Phys 2000;45:1032–41.
[49] Safa Y, Pfenniger D. Equation of state and stability of the helium-hydrogen mixture at cryogenic temperature. Eur Phys J B 2008;66:337–52.
[50] Mamedov B, Somuncu E. Analytical treatment of second virial coefficient over Lennard-Jones (2n-n) potential and its application to molecular systems. J Mol Struct 2014;1068:164–9.
[51] Cuadros F, Cachadiña I, Ahumada W. Determination of lennard-jones interaction parameters using a new procedure. Mol Eng 1996;6:319–25.
[52] Tchouar N, Benyettou M, Kadour F. Thermodynamic, structural and transport properties of lennard-jones liquid systems. a molecular dynamics simulations of liquid helium, neon, methane and nitrogen. Int J Mol Sci 2003;4:595–606.
[53] Chen RY, Yuen WYD. Short-time oxidation behavior of low-carbon, low-silicon steel in air at 850–1180 °C: II. linear to parabolic transition determined using existing gas-phase transport and solid-phase diffusion theories. Oxid Met 2010;73:353–73.
[54] Hobbs ML, Schmitt RG, Moffat HK. JCZS3–an improved database for EOS calculations. (SAND2018-6390C). Sandia National Laboratories; 2018,
[55] Mamedov BA, Somuncu E. Fully analytical evaluation of second virial coefficient with stockmayer potential and its applications. High Temp 2020;58:818–23.
[56] Kristóf T, Liszi J. Effective intermolecular potential for fluid hydrogen sulfide. J Phys Chem B 1997;101:5480–3.
[57] Heldmann J, Marinova M, Lim D, et al. Mission architecture using the spacex starship vehicle to enable a sustained human presence on mars. New Space 2022;10:259–73.
[58] Smith P, Golden D, Frenklach M, et al. GRI-mech 3.0. 2000, Version 3.0 http://combustion.berkeley.edu/.
[59] Yan C, Zhao H, Wang Z, Song G, Lin Y, Mulvihill CR, Jasper AW, et al. Low- and intermediate-temperature oxidation of dimethyl ether up to 100 atm in a supercritical pressure jet-stirred reactor. Combust Flame 2022;243:112059.
[60] Curran H, Gaffuri P, Pitz W, Westbrook C. A comprehensive modeling study of Iso-octane oxidation. Combust Flame 2002;129:253–80.
[61] Sun W, Chen Z, Gou X, Ju Y. A path flux analysis method for the reduction of detailed chemical kinetic mechanisms. Combust Flame 2010;157:1298–307.
[62] Wang Z, Thawko A, Mei B, Xu W, Law CK, Ju Y. Pressure effects on reactivity and extinction of N-dodecane diffusion cool flame. Combust Flame 2023;254:112829.
[63] Maruta K, Abe K, Hasegawa S, Maruyama S, Sato J. Extinction characteristics of CH4/CO2 versus O2/CO2 counterflow non-premixed flames at elevated pressures up to 0.7 MPa. Proc Combust Inst 2007;31:1223–30.
[64] Reuter CB, Zhang R, Yehia OR, Rezgui Y, Ju Y. Counterflow flame experiments and chemical kinetic modeling of dimethyl ether/methane mixtures. Combust Flame 2018;196:1–10.
[65] Reuter CB, Lee M, Won SH, Ju Y. Study of the low-temperature reactivity of large n-alkanes through cool diffusion flame extinction. Combust Flame 2017;179:23–32.
[66] Nilsson EJ, Van Sprang A, Larfeldt J, Konnov AA. The comparative and combined effects of hydrogen addition on the laminar burning velocities of methane and its blends with ethane and propane. Fuel 2017;189:369–76.
[67] Lowry W, Vries J, Krejci M, Petersen E, Serinyel Z, Metcalfe W, et al. Laminar flame speed measurements and modeling of pure alkanes and alkane blends at elevated pressures. J Eng Gas Turb. Pow. 2011;133:091501.
[68] Rozenchan G, Zhu D, Law C, Tse S. Outward propagation, burning velocities, and chemical effects of methane flames up to 60 ATM. Proc Combust Inst 2002;29:1461–70.
[69] Dahoe A, De Goey L. On the determination of the laminar burning velocity from closed vessel gas explosions. J Loss Prev Process Ind 2003;16:457–78.
[70] Daly CA, Simmie JM, Rmel JW. Burning velocities of dimethyl ether and air. Combust Flame 2001;125:1329–40.

[71] Qin X, Ju Y. Measurements of burning velocities of dimethyl ether and air premixed flames at elevated pressures. Proc Combust Inst 2005;30:233–40.
[72] Dirrenberger P, Glaude P, Bounaceur R, Le Gall H, Da Cruz AP, Konnov A, et al. Laminar burning velocity of gasolines with addition of ethanol. Fuel 2014;115:162–9.
[73] Davis SG, Law C. Determination of and fuel structure effects on laminar flame speeds of C_1 to C_8 hydrocarbons. Combust Sci Technol 1998;140:427–49.
[74] Jerzembeck S, Peters N, Pepiotdesjardins P, Pitsch H. Laminar burning velocities at high pressure for primary reference fuels and gasoline: experimental and numerical investigation. Combust Flame 2009;156:292–301.